MAGNETICALLY SUSPENDED LINEAR PULSE MOTOR FOR SEMICONDUCTOR WAFER TRANSFER IN VACUUM CHAMBER

Shin-ichi Moriyama, Naoji Hiraki
Kyushu Institute of Technology, 680-4, Kawazu, Iizuka, Fukuoka 820, Japan

Katsuhide Watanabe
Ebara Research Co., Ltd., 4-2-1, Honfujisawa, fujisawa, Kanagawa 251, Japan

Yoichi Kanemitsu
Kyushu University, 6-10-1, hakozaki, higashi-ku, Fukuoka 812-81, Japan

SUMMARY

This paper describes a magnetically suspended linear pulse motor for a semiconductor wafer transfer robot in a vacuum chamber. The motor can drive a wafer transfer arm horizontally without mechanical contact. In the construction of the magnetic suspension system, four pairs of linear magnetic bearings for the lift control are used for the guidance control as well. This approach allows us to make the whole motor compact in size and light in weight.

The tested motor consists of a double-sided stator and a transfer arm with a width of 50 mm and a total length of 700 mm. The arm, like a ladder in shape, is designed as the floating element with a tooth width of 4 mm (a tooth pitch of 8 mm). The mover mass is limited to about 1.6 kg by adopting such an arm structure, and the ratio of thrust to mover mass reaches to 3.2 N/kg under a broad air gap (1 mm) between the stator teeth and the mover teeth.

The performance testing was carried out with a transfer distance less than 450 mm and a transfer speed less than 560 mm/s. The attitude of the arm was well controlled by the linear magnetic bearings with a combined use, and consequently the repeatability on the positioning of the arm reached to about 2 μm. In addition, the positioning accuracy was improved up to about 30 μm through a compensation of the 128-step wave current which was used for the micro-step drive with a step increment of 62.5 μm.

INTRODUCTION

In the semiconductor manufacturing industries, the demand for a super clean robot without generation of dust particles and release of gas is increasing in connection with shifting the wafer

processes from a clean room to a vacuum chamber. One advantageous method for realizing such a robot is to drive a wafer transfer arm without mechanical contact by means of magnetic suspension techniques (ref.1). For example, we think of a three-dimensional robot as shown in Fig.1 (ref.2). The linear actuator comprises a linear motor and linear magnetic bearings and drives a wafer transfer arm horizontally. A floating body equipped with this actuator is rotatable in the horizontal plane by a rotary actuator, corresponding to a sort of outer rotor. The rotary actuator comprises a rotary motor, radial magnetic bearings and a passive thrust magnetic bearing, being driven vertically by a vertical feed screw assembly. The linear and rotary actuators are hermetically enclosed in a box-like case and a cylindrical wall respectively. Therefore we can operate this robot without any contamination of the vacuum environment in a wafer processing chamber.

In this work, we propose a magnetically suspended linear pulse motor (MSLPM) as the linear actuator of a wafer transfer robot as shown in Fig. 1. Selecting linear pulse motor from among candidate linear actuators is based on a view of precise wafer positioning by open-loop control and is advantageous to vacuum chamber robots which can hardly have sensors for locating the robot arms. In a design of the MSLPM, we must consider the following points. First, it is necessary to make the whole motor compact in size and light in weight because of reduction of the load on a floating body such as the outer rotor in Fig. 1. Second, the MSLPM is required to yield the desired thrust force against a broad air gap which must be arranged in consideration of a wall thickness of the box-like case. Last, the positioning of the arm has to be done with a high resolution from a viewpoint of continuous path control on wafer transfer robots. In this paper, we present a construction of the MSLPM satisfying these demands and discuss the performance.

CONSTRUCTION OF MSLPM

Figure 2 shows the basic structure of the MSLPM. The MSLPM consists of a linear pulse motor (LPM) and four pairs of upper and lower linear magnetic bearings (LMB) and has two features. One is that a ladder-like transfer arm is used as the floating mover of the MSLPM. We have to set a 1 mm air gap between the stator and the mover in consideration of a 0.5 mm wall thickness of the MSLPM case. Selecting such an arm structure is a countermeasure against a marked lowering of thrust force caused by the broad air gap. Another is that the LMB components, namely the electromagnet and the gap sensor, for the lift control are used for the guide control as well. By applying such a combined use, we can divide the MSLPM case into two parts and can realize compactness of the whole motor. The size of the MSLPM is roughly decided from the distance between center axes of the front and back electromagnets, h, and the width of the transfer arm, k. In consideration of an overall arrangement for the LPM and the LMB, we tried designing the MSLPM under the conditions $h = 164$ mm and $k = 50$ mm.

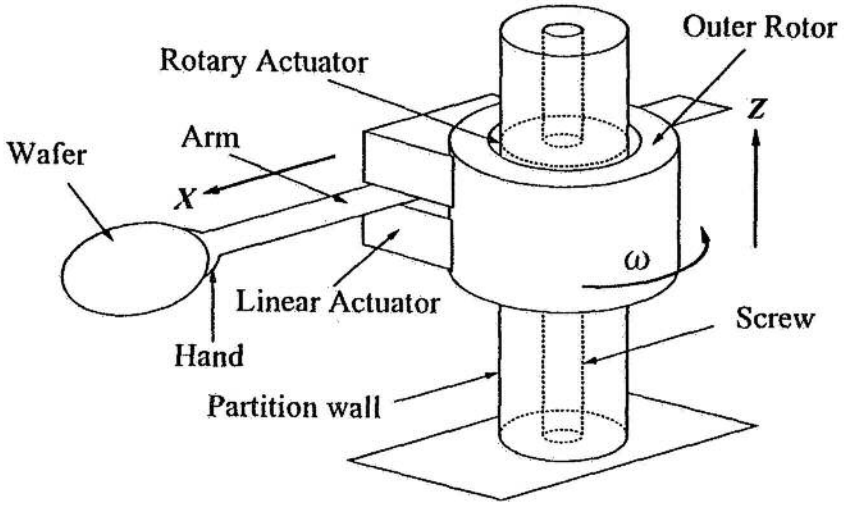

Figure 1. Conceptual diagram of a wafer transfer robot in a vacuum chamber.

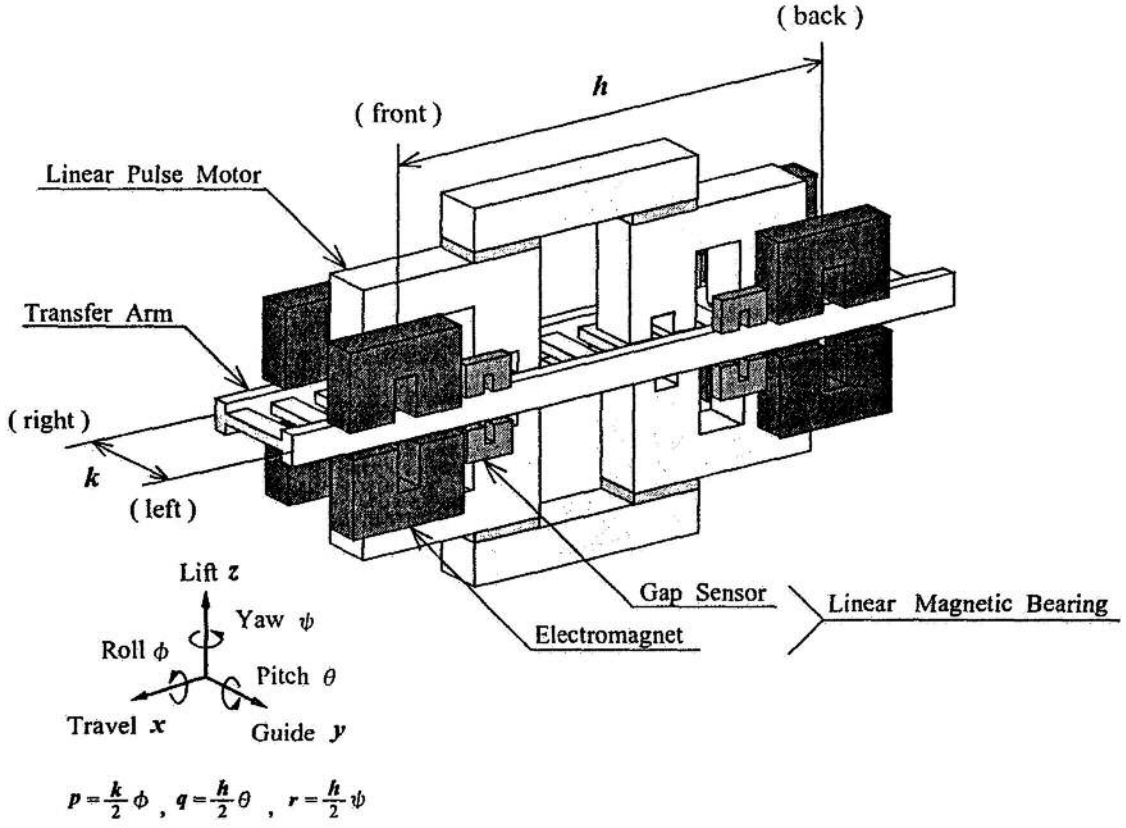

Figure 2. Basic structure of the MSLPM.

The MSLPM is a type of double sided LPM and has a cross sectional structure as shown in Fig.3. There are rungs of the ladder-like arm, namely teeth of the mover alone, between upper and lower parts of the stator. The tooth pitch determining the positioning resolution is twice the tooth width ($2a$). Four permanent magnets inserted in the stator produce a magnetic flux represented by the dotted lines. On the other hand, two pairs of upper and lower electromagnets, namely the A-phase electromagnet with an exciting current I_A and the B-phase one with I_B, form a magnetic flux represented by the solid lines. Therefore, if the total magnetic flux penetrating the mover is efficiently distributed at the tooth region other than the air space, it is possible for the stator to generate the required thrust force in the x -direction. From this point, it is better for the mover tooth to satisfy the condition t (thickness) $\geq a$ (width) $>> \delta$ (gap length). But at the same time we have to consider that the mover mass is larger with t and the positioning resolution is lower with a . Figure 4 shows the typical result of a 2-dimensional magnetic field analysis for the conditions $t = a = 4$ mm and $\delta = 1$ mm. In this analysis, we suppose that the A-phase current is supplied alone. It is found that the magnetic flux is efficiently centered at the two mover teeth under the left magnetic pole of the A-phase electromagnet. From such analytical results, we adopted the above-mentioned tooth dimensions for the ladder-like arm.

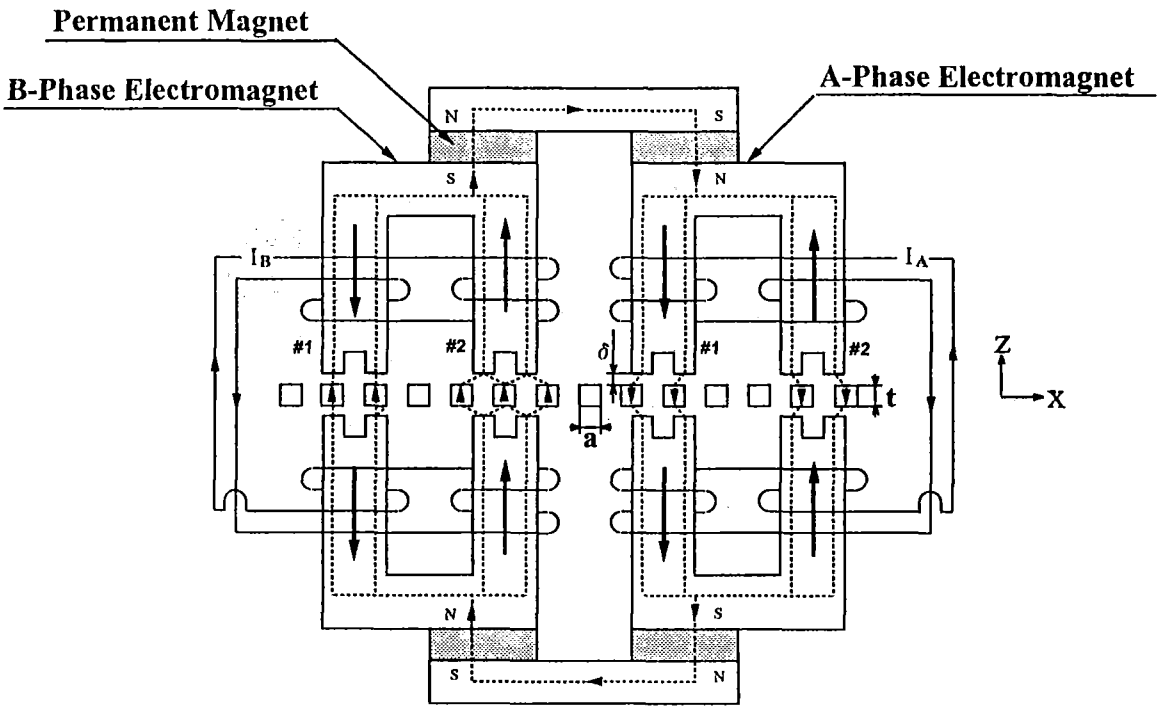

Figure 3. Cross sectional structure of the LPM.

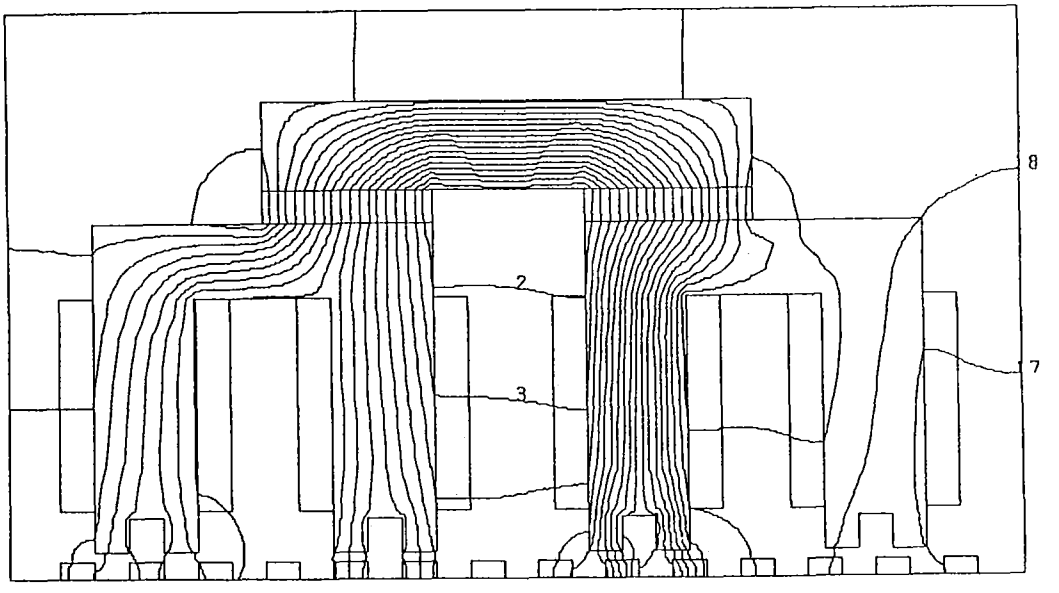

Figure 4. Magnetic flux distribution of the LPM.

In Fig.2, the four pairs of electromagnets are used for the attitude control with five degrees of freedom, that is, lifting (z), guiding (y), rolling (p), pitching (q) and yawing (r). Figure 5 shows a cross section of the two pairs installed at the front of the transfer arm or at the back. The electromagnets are arranged so that the center axes of them can be coincided with both edges of the arm. They are distinguished by the suffixes u (upper), d (lower), l (left), r (right), b (back) and f (front). The clearance between an electromagnet and the arm is expressed with the gap length $\delta_{ij}^{u(d)}$ and the stagger length λ_{ij} as

$$\delta_{ij} = \frac{1}{2}\left(\delta_{ij}^{u} - \delta_{ij}^{d}\right) = \delta_{ij}^{u} - \delta_{0} = \delta_{0} - \delta_{ij}^{d} \tag{1}$$

$$\lambda_{j} = \frac{1}{2}\left(\lambda_{lj} - \lambda_{rj}\right) = \lambda_{lj} - \lambda_{0} = \lambda_{0} - \lambda_{rj} \tag{2}$$

where $i = l, r$, $j = b, f$ and δ_0, λ_0 are the desired values. The attraction force which a pair of upper and lower electromagnets yields in the lifting direction is given by

$$f_{ij} = f_{ij}^{u} - f_{ij}^{d} \sim 2N\delta_{ij} + 2KI_{ij} \tag{3}$$

$$I_{ij} = \frac{1}{2}\left(I_{ij}^{u} - I_{ij}^{d}\right) \tag{4}$$

where N and K are the differential coefficients with respect to the gap length $\delta_{ij}^{u(d)}$ and the exciting current $I_{ij}^{u(d)}$ respectively. The attraction force which the two pairs yield in the

guiding direction is given by

$$f_{Tj}=f_{Tlj}^{u}+f_{Tlj}^{d}-f_{Trj}^{u}-f_{Trj}^{d}\sim 4N_T\lambda_j+4K_T I_{Tj} \tag{5}$$

$$I_{Tj}=\frac{1}{2}\left(I_{lj}^{u}+I_{lj}^{d}\right)-I_0=I_0-\frac{1}{2}\left(I_{rj}^{u}+I_{rj}^{d}\right) \tag{6}$$

where N_T and K_T are the differential coefficients with respect to the stagger length λ_{ij} and the exciting current $I_{ij}^{u(d)}$ respectively and I_0 is a bias current to feed the required attraction force to an electromagnet. From Eqs (1) ~ (6), we get the following controllable forces related to the attitude control:

$$f_z=f_{lb}+f_{rb}+f_{lf}+f_{rf}=-8Nz+8KI_z \tag{7}$$

$$f_p=f_{lb}-f_{rb}+f_{lf}-f_{rf}=-8Np+8KI_p \tag{8}$$

$$f_q=f_{lb}+f_{rb}-f_{lf}-f_{rf}=-8Nq+8KI_q \tag{9}$$

$$f_y=f_{Tb}+f_{Tf}=-8N_T y+8K_T I_y \tag{10}$$

$$f_r=-f_{Tb}+f_{Tf}=-8N_T r+8K_T I_r \tag{11}$$

where $z\sim r$ and $I_z\sim I_r$ are defined with the clearance variables δ_{ij}, λ_j and the current variables I_{ij}, I_{Tj} respectively. The above equations indicate that we can construct the five feedback loops against the attitude displacements $z\sim r$ through converting the supposed current variables $I_z\sim I_r$ to the real exciting currents I_{ij}^{u}, I_{ij}^{d}.

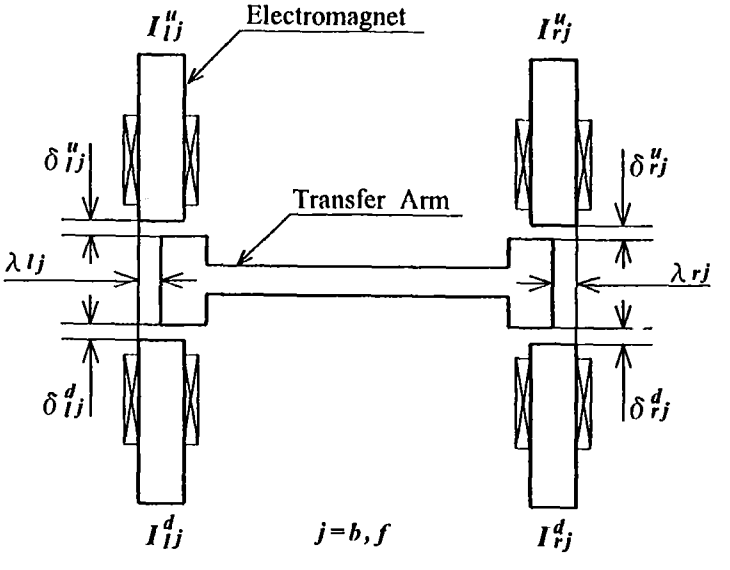

Figure 5. Cross sectional structure of the LMB electromagnets.

On the other hand, the four pairs of gap sensors in Fig.2 are used for the detection of the attitude displacements $z \sim r$. They are installed with the same arrangement as the electromagnets in Fig.5. Figure 6 shows a double-bridged circuit for the two pairs of sensors. The circuit involves the four sensors and the six resistors which are symbolized by the inductances L_{ij}^{u}, L_{ij}^{d} and the resistances $R \sim 4R$ respectively. The inductance given by

$$L_{ij}^{u(d)} \sim L_0 + \alpha\left(\delta_{ij}^{u(d)} - \delta_0\right) + \alpha_T\left(\lambda_{ij} - \lambda_0\right) \tag{12}$$

leads to the output signals

$$\hat{\delta}_{ij} \sim -\frac{GS_0\alpha}{L_0}\delta_{ij} \tag{13}$$

$$\hat{\lambda}_j \sim -\frac{G_T S_0 \alpha_T}{L_0}\lambda_j \tag{14}$$

where α and α_T are the differential coefficients with respect to the gap length $\delta_{ij}^{u(d)}$ and the stagger length λ_{ij} respectively and L_0 is the desired value. Since the signals $\hat{\delta}_{ij}$ and $\hat{\lambda}_j$ are proportional to the clearance variables δ_{ij} and λ_j respectively, we can easily convert them to the attitude displacements $z \sim r$.

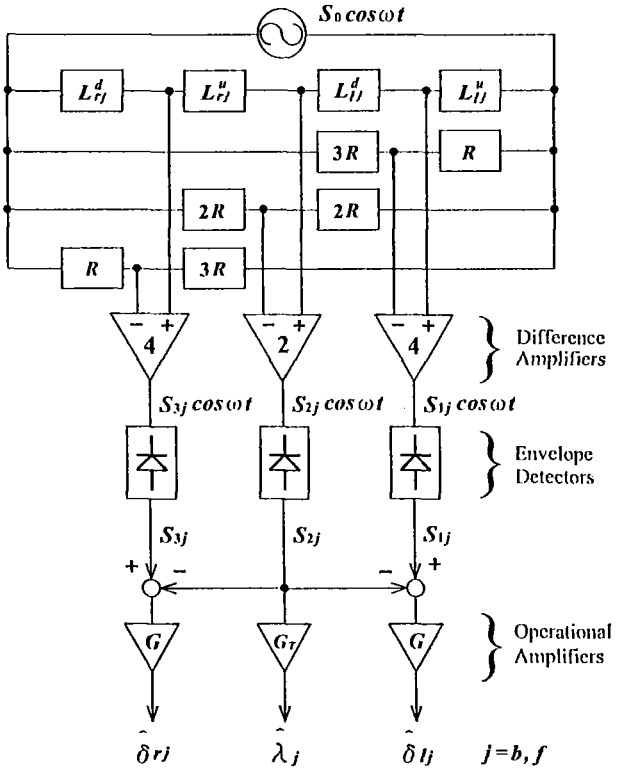

Figure 6. A double-bridged circuit for the gap sensors.

PERFORMANCE TEST

We made a MSLPM stator and a transfer arm as a trial. Figure 7 shows an apparatus for examining the performances of the tested MSLPM. The two stator parts are put in the upper and lower cases respectively. We could restrict the inside volume of each case to 212 mm by 74 mm by 61 mm. The arm has a total length of 700 mm and is movable to an optional position less than 450 mm. We also could limit the mass of the arm to 1.56 kg. The laser displacement meter is used for measuring the location of the arm over the performance test, and the load cell is used only for measuring the static thrust force of the MSLPM.

The performance test was carried out with two controllers as shown in Fig.7. The LPM controller forms an open-loop drive system for the micro-step positioning of the arm. The microprocessor supplies the command of the transfer speed, $\hat{v}$. And the logic sequencer produces the signals of the A-phase and B-phase exciting currents, $\hat{I}_A$ and $\hat{I}_B$, and the count of a series of timing pulses, $\hat{x}$. The count $\hat{x}$ is returned to the microprocessor as the positioning signal. If it reaches to the set position $\hat{x}_0$, then the command $\hat{v}$ is turned off. The timing pulses are generated at a frequency proportional to the command $\hat{v}$. The signals $\hat{I}_A$ and $\hat{I}_B$ change by each timing pulse according to waveform data stored in two read-only-memories beforehand. As a result, the LPM electromagnets are magnetized by 128-step wave currents and the arm is located by the micro-step drive with a step increment of $2a$ / 128 (62.5 μm).

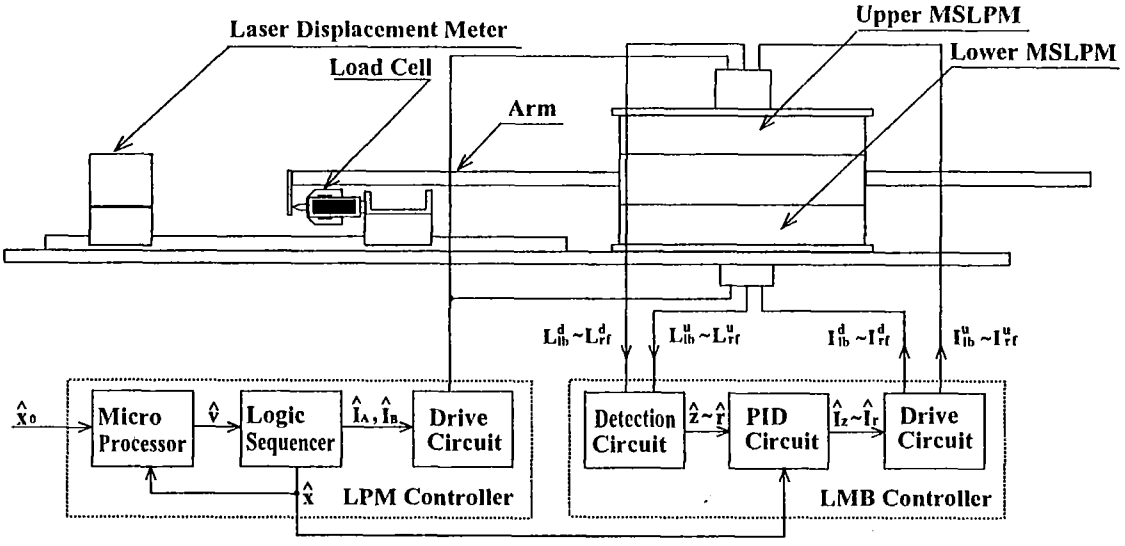

Figure 7. An apparatus for the performance test.

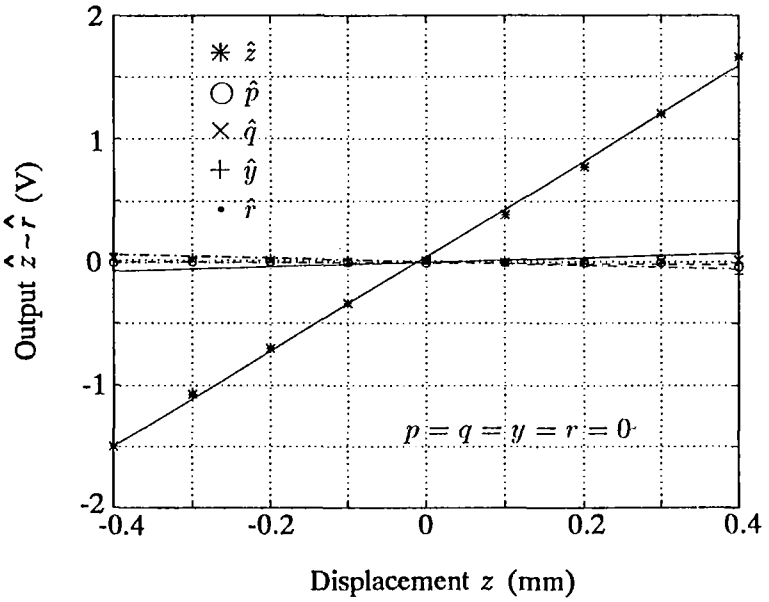

Figure 8. Dependence of output signals on the displacement z.

On the other hand, the LMB controller forms a feedback system for the attitude control of the arm. The detection circuit, which includes double-bridged circuits as shown in Fig.5, produces the displacement signals $\hat{z} \sim \hat{r}$, and the PID (proportional-integral-differential) circuit produces the control signals $\hat{I}_z \sim \hat{I}_r$. Regarding the signal $\hat{I}_q$, the positioning signal $\hat{x}$ from the LPM controller is considered to cancel an unbalance force in the pitching direction. The drive circuit controls the current of each LMB electromagnet according to the signals $\hat{I}_z \sim \hat{I}_r$, and consequently the arm is magnetically supported with a standard attitude. We carried out a calibration of the detection circuit before the performance test. We supported the arm by four micrometers in the lifting direction and by two in the guiding direction, and then moved in each direction of $z \sim r$. Figure 8 shows the typical result of the calibration. For the movement only in the z-direction, the signal $\hat{z}$ increases in proportion to the displacement z and the other signals are little produced. We obtained the same results for the signals $\hat{y} \sim \hat{r}$. We also estimated the following sensitivity from the inclination of a fitted line as shown in Fig.8: 3.95 V/mm for $\hat{z}$, 3.25 V/mm for $\hat{p}$, 1.89 V/mm for $\hat{q}$, 2.01 V/mm for $\hat{y}$ and 1.14 V/mm for $\hat{r}$.

The static thrust characteristic is one of fundamental performances of the MSLPM and must be estimated accurately. So we first measured the static thrust force while suspending the arm by the LMB. Figure 9 shows the typical results. There is little difference between the A-phase thrust force and the B-phase one. The maximum thrust force at $I_A = 0.7$ A or at $I_B = 0.7$ A can be estimated to 5.1 N. Thus the ratio of thrust force to mover mass becomes 3.2 N/kg.

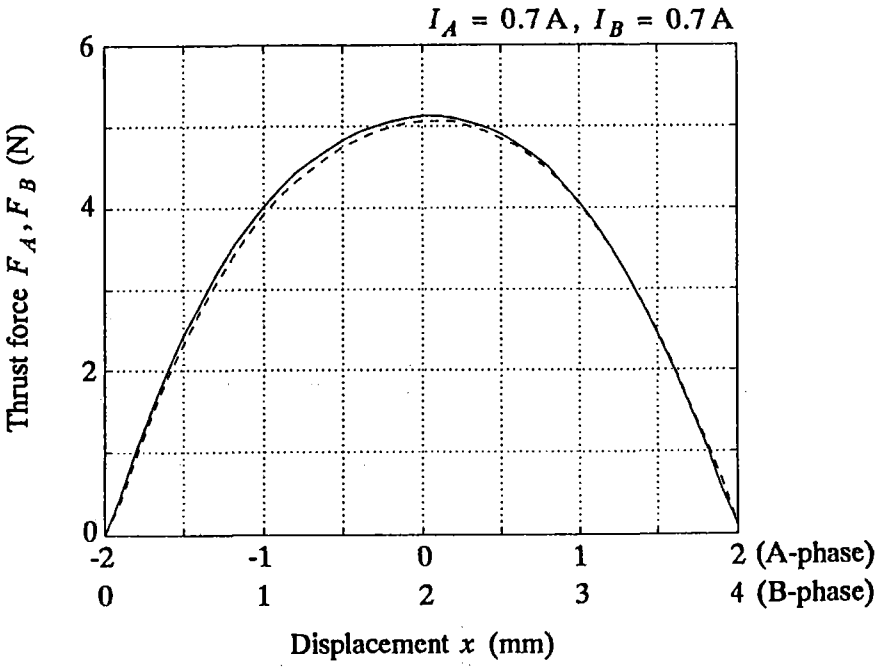

(a) Static thrust force versus displacement.

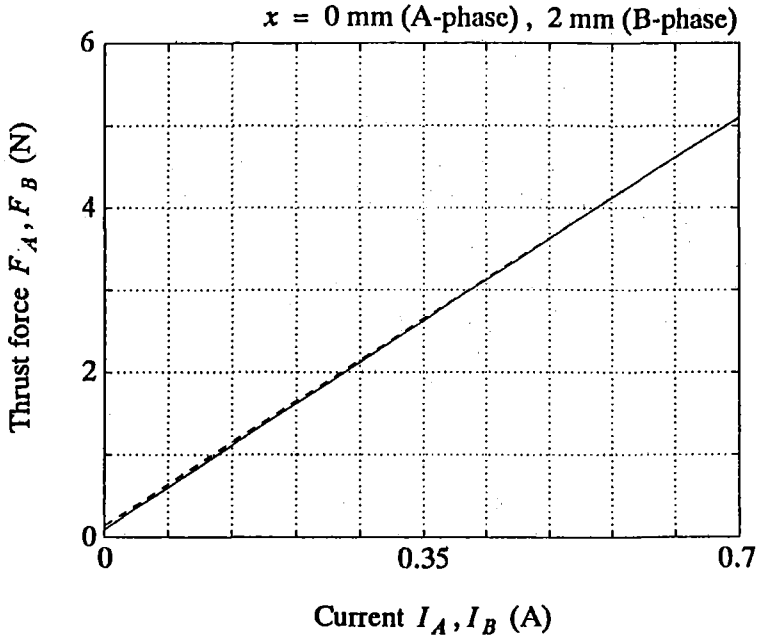

(b) Static thrust force versus exciting current.

Figure 9. Static thrust characteristics of the MSLPM. The solid and dotted lines indicate a A-phase force and a B-phase one respectively.

From the measuring results shown in Fig.9, we can express the thrust forces as

$$F_A = I_A \left\{ K_1 \cos\left(\pi \frac{x}{a}\right) - K_3 \cos\left(3\pi \frac{x}{a}\right) \right\} \tag{15}$$

$$F_B = I_B \left\{ K_1 \sin\left(\pi \frac{x}{a}\right) + K_3 \sin\left(3\pi \frac{x}{a}\right) \right\} \tag{16}$$

where $K_1 = 7.7$ A/N and $K_3 = 0.4$ N/A. In the above equations, each second term on the right hand side is regarded as a third harmonic component on the static thrust versus displacement characteristic. Here we neglect the third harmonic component because $K_3 << K_1$, and insert the sine wave currents

$$I_A = I_1 \sin\left(\pi \frac{\hat{x}}{a}\right) \tag{17}$$

$$I_B = -I_1 \cos\left(\pi \frac{\hat{x}}{a}\right) \tag{18}$$

to Eqs (15) and (16). Consequently, we can express the work load on the total thrust force $F = F_A + F_B$ as

$$\int_x^{x+a} F_1 \sin\left(\pi \frac{\hat{x}}{a} - \pi \frac{x}{a}\right) \mathrm{d}\hat{x} = \frac{1}{2} m \left(\frac{\mathrm{d}x}{\mathrm{d}t}\right)^2 \tag{19}$$

where $F_1 = K_1 I_1 = 5.4$ N and m is the mover mass. From the above equation, the starting speed

$$v_0 = \left(\frac{4\,a\,F_1}{\pi m}\right)^{1/2} \tag{20}$$

is derived, being estimated to 133 mm/s. Since the maximum slewing speed generally becomes several times the starting speed, we can expect a transfer speed of 300 mm/s to 500 mm/s.

Next, we examined the performances on the traveling of the arm. Figure 10 shows the typical results. The arm is accelerated up to a speed of 300 mm/s under the sine wave excitation as given by Eqs. (17) and (18), and then it is stopped at a set position of 400 mm after the slowdown to a waiting speed. The arm also is moved in reverse with the same speed pattern, and then it is returned at the original position. In this round trip, though the arm seems to be significantly displaced from the standard attitude in the r-direction, the displacement is smaller than the allowable value. Thus it can be said that the arm is moving horizontally while keeping sufficient clearance for the upper and lower cases. We carried out round trips and measured the stop position every time the arm was returned. As a result, the repeatability was estimated to about 2μm. Furthermore, we examined a limit of the steady speed in a trapezoidal speed pattern as shown in Fig. 10, and consequently obtained a maximum speed of 560 mm/s. On the other hand, the maximum speed measured with a step-speed pattern, namely the starting speed, was 125 mm/s. It is in good agreement with the expected value mentioned in the previous paragraph. This suggests that a work load of the MSLPM to the arm is perfectly converted into a kinetic energy of the arm. This ideal energy transformation together with the excellent repeatability may be a remarkable feature of the MSLPM.

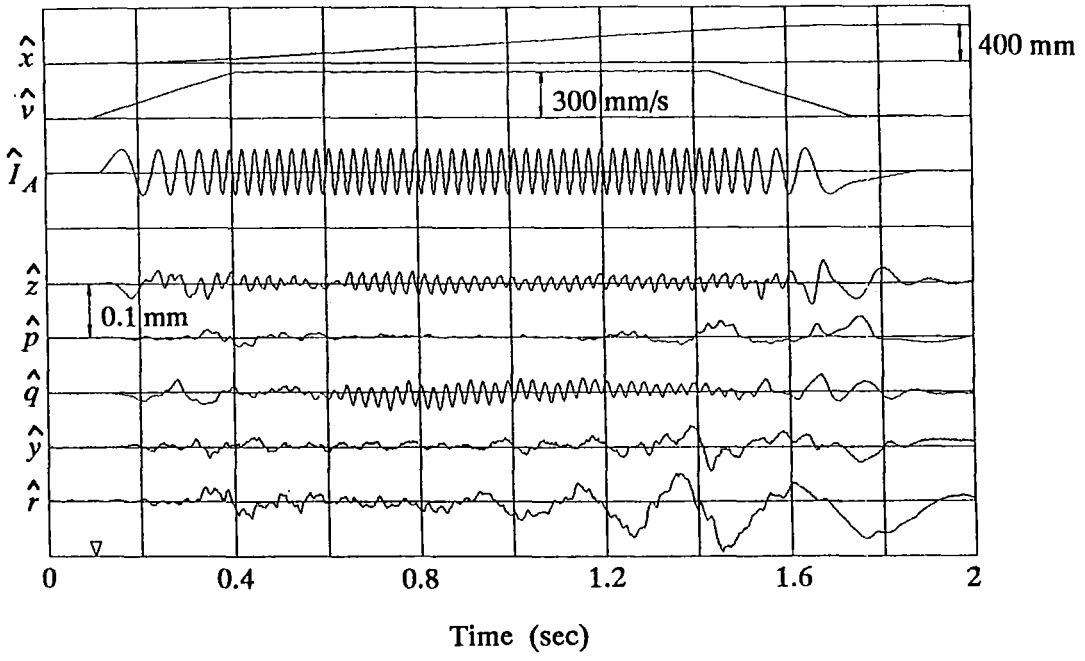

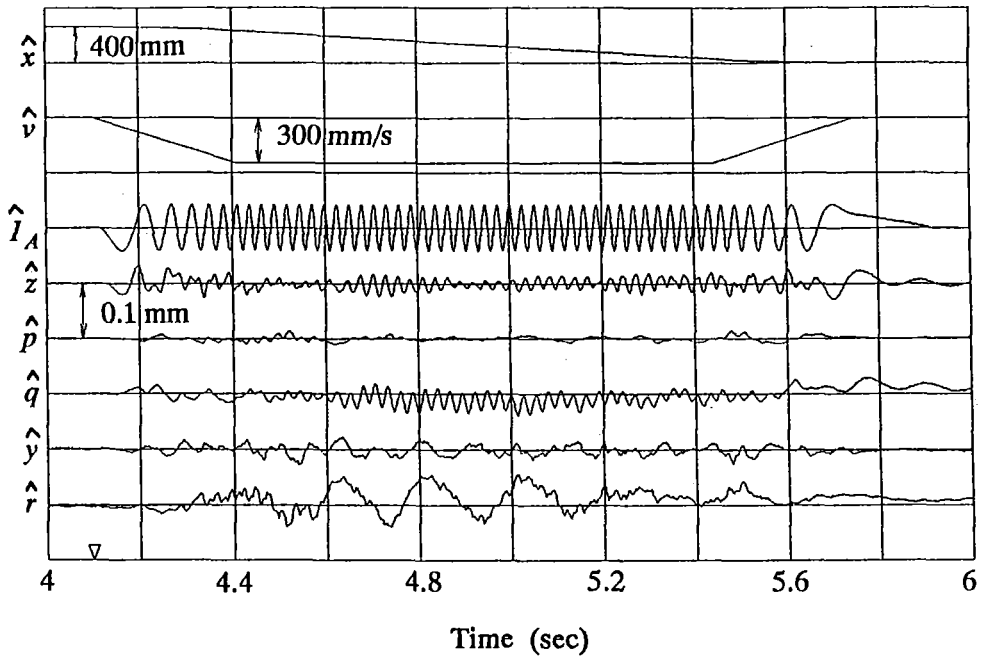

Figure 10. Time evolution of the positioning signal $\hat{x}$, the speed command $\hat{v}$, the A-phase signal $\hat{I}_A$ and the displacement signals $\hat{z} \sim \hat{r}$ during traveling the arm forward and backward. Each displacement of $z \sim r$ is expressed with a scale of 0.1mm/div. and the allowable value determined by the clearance between the arm and the MSLPM cases is as follows: ± 0.5 mm for z, ± 0.58 mm for p, ± 0.26 mm for q, ± 1.0 mm for y, ± 0.51 mm for r.

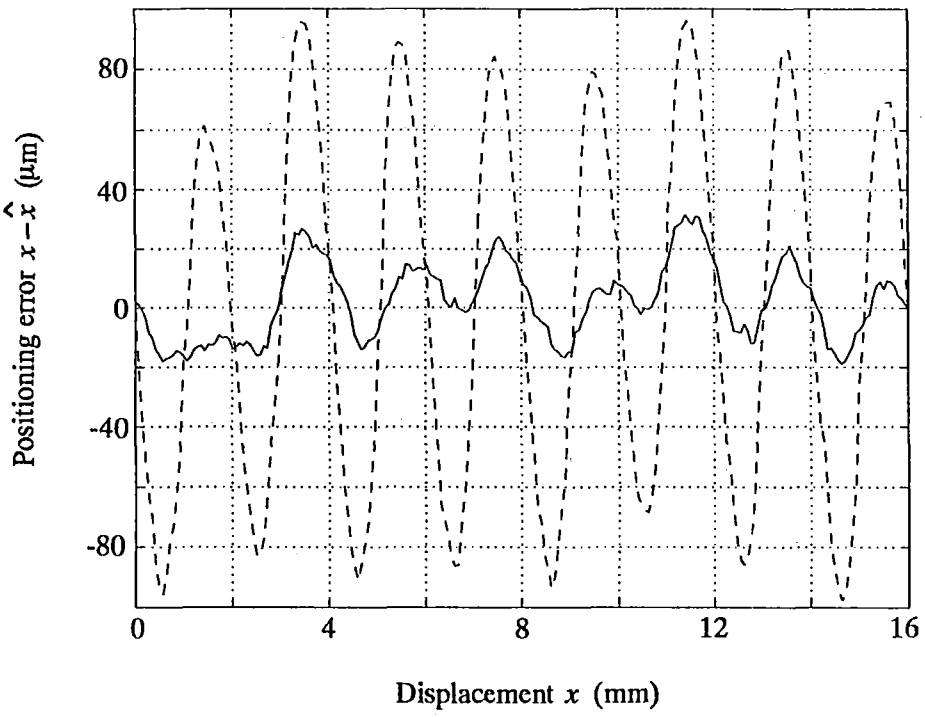

Figure 11. Positioning error on the micro-step drive. The dotted and solid curves indicate a step error for the sine wave excitation and one for the compensated excitation respectively.

Lastly, we examined the positioning error of the micro-step drive due to the sin wave excitation. As a result, it was found that there was a periodical error as shown by the dotted curve in Fig.11. The amplitude of the error $x-\hat{x}$ is more than the step increment of the micro-step drive. It is inferred that such an error is mainly due to a mismatching between the sine wave currents and the static thrust characteristics. From Eqs (15) ~ (18), the total thrust force involving the third harmonic component can be expressed by

$$F = F_1 \sin\left(\pi\frac{\hat{x}}{a} - \pi\frac{x}{a}\right) - F_3 \sin\left(\pi\frac{\hat{x}}{a} + 3\pi\frac{x}{a}\right) \tag{21}$$

where $F_3 = K_3 I_1 = 0.3\,\mathrm{N}$. Considering the condition $|x-\hat{x}| << a$ at $F=0$, we can find that there is a periodical error with the period $a/2$ (2 mm) and the amplitude $a F_3/\pi F_1$ (70 μm). This supposed error is similar to the measured one.

The positioning error due to the static thrust characteristics can be reduced by matching the exciting currents with higher-order harmonic components. The exciting currents matched with the third harmonic components in Eqs (15) and (16) are given by

$$I_A = I_1 \sin\left(\pi\frac{\hat{x}}{a}\right) + I_3 \tan\left(\pi\frac{\hat{x}}{a}\right)\cos\left(3\pi\frac{\hat{x}}{a}\right) \tag{22}$$

$$I_B = -I_1 \cos\left(\pi \frac{\hat{x}}{a}\right) + I_3 \cot\left(\pi \frac{\hat{x}}{a}\right) \sin\left(3\pi \frac{\hat{x}}{a}\right) \tag{23}$$

where $I_3 = I_1 K_3 / K_1$. The above equations lead to the ideal thrust forces without third harmonic component under the conditions $|K_3| << K_1$ and $|x - \hat{x}| << a$. By applying such a compensation to the 128-step wave currents, the positioning error became less than 30 μm, as shown by the solid curve in Fig.11.

CONCLUSION

We have constructed the magnetically suspended linear pulse motor in order to develop the linear actuator suitable to a wafer transfer robot in the ultra-high vacuum environment. The features and performances are as follows.

(1) The linear magnetic bearings combining the lift control and the guide control are used in the magnetic suspension system. By omitting them for the guide control, the case used for enclosing this motor hermetically can be divided into two parts. This is advantageous to a compactness of the linear actuator.

(2) The floating mover is the ladder-like arm with a total length of 700 mm and a width of 50 mm. The tooth width (pitch) is 4 mm (8 mm) and the air gap length is 1 mm. By adopting this arm, the mover mass is limited to about 1.6 kg and the ratio of thrust to mover mass reaches to 3.2 N/kg under the broad air gap.

(3) The attitude of the arm is well controlled by the magnetic suspension system, and consequently the clearance between the arm and the case is sufficiently maintained even during translation of the arm.

(4) The arm is horizontally movable with a transfer distance less than 450 mm and a transfer speed less than 560 mm/s by means of the micro-step positioning system. The positioning resolution, namely the step increment of the micro-step drive, is 62.5 μm. The positioning repeatability is about 2 μm and the positioning accuracy is about 30 μm. The performances indicate that this motor is sufficiently applicable to the wafer transfer robot.

REFERENCES

1. Ota, M.; Andoh, S.; and Inoue, H.: Mag-Lev Semiconductor Wafer Transporter for Ultra-High-Vacuum Environment, *Proc. 2nd Int Symp. on Magnetic Bearings*, July 12-14, 1990, pp. 109-114.
2. Wtanabe, K.; Kanemitsu, Y.; Shinozaki, H.; Hiraki, N.; and Moriyama, S.: Robot with Dust-Free and Maintenance-Free Actuators, US Patent 5,397,212.